PLOS ONE

High Spatial Resolution and Temporally Resolved T$_2$* Mapping of Normal Human Myocardium at 7.0 Tesla: An Ultrahigh Field Magnetic Resonance Feasibility Study

Fabian Hezel[1], Christof Thalhammer[1], Sonia Waiczies[1,2], Jeanette Schulz-Menger[1,2,3], Thoralf Niendorf[1,2]*

1 Berlin Ultrahigh Field Facility (B.U.F.F.), Max Delbrueck Center for Molecular Medicine, Berlin, Germany, 2 Experimental and Clinical Research Center, a Joint Cooperation between the Charité Medical Faculty and the Max Delbrueck Center for Molecular Medicine, Campus Berlin Buch, Berlin, Germany, 3 Department of Cardiology and Nephrology, HELIOS Klinikum Berlin Buch, Berlin, Germany

Abstract

Myocardial tissue characterization using T$_2$* relaxation mapping techniques is an emerging application of (pre)clinical cardiovascular magnetic resonance imaging. The increase in microscopic susceptibility at higher magnetic field strengths renders myocardial T$_2$* mapping at ultrahigh magnetic fields conceptually appealing. This work demonstrates the feasibility of myocardial T$_2$* imaging at 7.0 T and examines the applicability of temporally-resolved and high spatial resolution myocardial T$_2$* mapping. In phantom experiments single cardiac phase and dynamic (CINE) gradient echo imaging techniques provided similar T$_2$* maps. In vivo studies showed that the peak-to-peak B$_0$ difference following volume selective shimming was reduced to approximately 80 Hz for the four chamber view and mid-ventricular short axis view of the heart and to 65 Hz for the left ventricle. No severe susceptibility artifacts were detected in the septum and in the lateral wall for T$_2$* weighting ranging from TE = 2.04 ms to TE = 10.2 ms. For TE > 7 ms, a susceptibility weighting induced signal void was observed within the anterior and inferior myocardial segments. The longest T$_2$* values were found for anterior (T$_2$* = 14.0 ms), anteroseptal (T$_2$* = 17.2 ms) and inferoseptal (T$_2$* = 16.5 ms) myocardial segments. Shorter T$_2$* values were observed for inferior (T$_2$* = 10.6 ms) and inferolateral (T$_2$* = 11.4 ms) segments. A significant difference (p = 0.002) in T$_2$* values was observed between end-diastole and end-systole with T$_2$* changes of up to approximately 27% over the cardiac cycle which were pronounced in the septum. To conclude, these results underscore the challenges of myocardial T$_2$* mapping at 7.0 T but demonstrate that these issues can be offset by using tailored shimming techniques and dedicated acquisition schemes.

Competing Interests: TN is founder of MRI.Tools GmbH. This does not alter the authors' adherence to all the PLOS ONE policies on sharing data and materials. The authors would also like to point out that there are no patents, products in development or marketed products to declare.

* E-mail: Thoralf.Niendorf@mdc-berlin.de

Introduction

Emerging cardiovascular magnetic resonance (CMR) imaging applications include T$_2$* relaxation sensitized techniques, which are increasingly used in basic research and (pre)clinical imaging. Methodological developments in T$_2$* sensitized imaging [1–4] and simulations of myocardial vasculature [5,6] have been indispensable. Applications include investigation of the microstructure of the isolated rat heart [7], detection of myocardial ischemia [8–14], probing of vasodilator or dipyridamole-induced changes in myocardial perfusion [15–18], visualization of scarred myocardium [19], imaging of capillary recruitment [20] and assessment of tissue oxygenation related to endothelium-dependent blood flow changes [21]. T$_2$* mapping has also been shown to be of substantial clinical value for the ascertainment of myocardial iron levels [22–29].

The most widely used methods for T$_2$* mapping are echo planar imaging (EPI) and gradient echo based techniques. Unlike conventional CINE gradient echo imaging, the relatively strong T$_2$*-weighting required to make gradient echo sequences sensitive to changes in magnetic susceptibility asks for a long evolution time (TE) between RF excitation and data acquisition. Consequently, gradient echo based myocardial T$_2$* mapping is commonly restricted to a single slice and single cardiac phase that can be accommodated in a single breath-hold at 1.5 T and 3.0 T [30–32].

The linear relationship between magnetic field strength and microscopic susceptibility [33–35] renders it conceptually appealing to pursue myocardial T$_2$* mapping at ultrahigh magnetic field strengths. Realizing the opportunities and challenges of T$_2$* mapping, this pilot study demonstrates the feasibility of ultrahigh field susceptibility-weighted myocardial imaging and examines its applicability for temporally-resolved and high spatial resolution myocardial T$_2$* mapping at 7.0 T. To meet this goal, the applicability of 2D spoiled gradient-echo multi-echo based techniques for T$_2$* mapping at 7.0 T is closely investigated in phantom experiments. The feasibility of gradient-echo multi-echo based techniques for fast CINE T$_2$* mapping of the human heart is

demonstrated at 7.0 T. We also present the suitability of this technique for high spatial resolution myocardial T$_2$* mapping by using thin slices (slice thickness = 2.5 mm) and in-plane spatial resolution of (1.1×1.1) mm^2. Our initial volunteer studies serve as a mandatory precursor to a broader clinical study. The merits and limitations of T$_2$* mapping using 2D spoiled gradient-echo multi-echo imaging at 7.0 T are discussed and implications for cardiac MR at 7.0 T are considered.

Methods

MR-Hardware

Imaging was conducted using a 7.0 T whole body MR scanner (Magnetom, Siemens Healthcare, Erlangen, Germany) equipped with a gradient system (Avanto, Siemens Healthcare, Erlangen, Germany) capable of supporting a slew rate of 200 mT/m/ms and a maximum gradient strength of 40 mT/m. A 16 channel transmit/receive coil array was used for excitation and signal reception. The coil was designed for cardiac imaging and comprises an anterior and posterior former, each laid out on a two-dimensional 2 by 4 grid of loop elements. For further details about the coil please see [36,37]. An MR stethoscope (EasyACT, MRI.TOOLS GmbH, Berlin, Germany) was used for cardiac triggering [38,39].

T$_2$* Mapping Techniques

Myocardial T$_2$* mapping is commonly conducted with cardiac triggered, segmented multi-echo spoiled gradient echo (**ME**) techniques that use breath-held acquisitions for respiratory motion compensation [8,9,15,18,40]. In this work, various ME configurations have been used for (i) time resolved CINE and for (ii) single cardiac phase acquisitions (Figure 1).

For single cardiac phase imaging, the acquisition period is commonly placed into end-diastole, which limits the viable window of data acquisition to 100 ms to 200 ms. Data acquisition is segmented over a series of cardiac cycles with each segment acquiring a set of echoes during the quiescent interval (Figure 1a). The number of segments and echoes per segment are dictated by the longest TE used for T$_2$* weighting as outlined in Figure 1a. To avoid T$_2$* errors due to signal modulations induced by fat-water phase shift, it is essential to choose echo times where fat and water are in-phase [4]. At 1.5 T and 3.0 T TE increments equivalent to the fat-water shift are 4.4 ms and 2.2 ms, respectively. At 7.0 T this inter echo time is 1.02 ms, which is beneficial for rapid multi-echo acquisitions. However, if a larger data matrix size is needed for high spatial resolution T$_2$* mapping, the readout/acquisition window can easily exceed 1.02 ms even when short dwell times are used. Consequently, it is elusive to accomplish inter-echo time increments of 1.02 ms for high spatial resolution T$_2$* mapping at 7.0 T using sequential multi echo gradient echo imaging.

CINE T$_2$* mapping might be feasible at 7.0 T assuming a T$_2$* reduction at 7.0 T versus 1.5 T and 3.0 T and considering the relationship between proper T$_2$* weighting and range of echo times to be covered. To this end, a maximum TE = 10 ms would be compatible with the needs of CINE imaging but would also provide sufficient coverage of the T$_2$* decay at 7.0 T.

For all these reasons, two imaging strategies were employed at 7.0 T:

i. Interleaved multi-shot multi-echo (**MS**) gradient echo technique for single cardiac phase myocardial T$_2$* mapping (Figure 1b). This approach addresses the competing constraints of inter echo time and spatial resolution of the **ME**

approach by adding more excitations and by interleaving the echoes.

ii. Multi-breath-hold multi-echo (**MB CINE**) gradient echo technique for CINE myocardial T$_2$* mapping (Figure 1c). This approach runs the trait that all k-space lines required to form the final image for a given echo time are acquired in a single breathhold.

Phantom Studies

For the evaluation of **MS** and **MB CINE** T$_2$* mapping strategies, phantom experiments were conducted using a long T$_2$* and medium T$_2$* phantom. For long T$_2$*, a cylindrical water phantom (diameter = 15 cm) containing an agarose copper sulfate solution (4 g CuSO$_4$ +2 g NaCl +2 g agarose dissolved in 1.0 l H$_2$O) was used. A glass capillary (inner diameter = 0.5 mm) filled with air and a tube (inner diameter = 5 mm) filled with water were placed inside the phantom to create strong susceptibility gradients of limited spatial extension within the uniform phantom. For the medium T$_2$* phantom, a cylindrical water phantom (diameter = 8 cm) containing agarose (5 mg agarose dissolved in 250 ml H$_2$O) was used. T$_2$* was reduced by ultrasmall superparamagnetic iron oxide particles (500 μl Molday ION (10 mg Fe/ml), BioPal, Worchester, USA), which afforded a T$_2$* of approximately 20 ms.

In the phantom experiments, **MS** (Figure 1b) and **MB CINE** (Figure 1c) T$_2$* mapping strategies were benchmarked against other T$_2$* mapping techniques, which are already established at 1.5 T and 3.0 T but are unsuitable for myocardial T$_2$* mapping at 7.0 T due to echo time and acquisition time constraints. These reference methods include:

i. conventional multi-echo (**ME**) gradient echo for single cardiac phase T$_2$* mapping (Figure 1a).

ii. multi-echo CINE (**ME CINE**) gradient echo (Figure 1d).

iii. multi-shot multi-echo CINE (**MS CINE**) gradient echo (Figure 1e).

For phantom T$_2$* mapping, an image matrix of 320×240, a field of view of (360×270) mm^2, an in-plane resolution of (1.1×1.1) mm^2, and a slice thickness ranging from 2.5 mm to 8 mm were used. A unipolar readout using gradient flyback was applied together with echo times ranging from 2.04 ms to 10.20 ms. This approach results in nine equidistant echoes with an inter echo time of 1.02 ms with the exception of **ME** and **ME CINE** due to gradient switching induced peripheral nerve stimulation constraints. For **ME** and **ME CINE** 6 echoes with an inter echo time of 3.06 ms and a TE$_{min}$ = 2.04 ms were used. For the **MS**, **MS CINE** and **MB CINE** techniques three excitations together with 3 echoes were used to ensure an inter-echo time of 1.02 ms. With the first excitation echo 1, 4 and 7 were acquired. The second excitation covered echo 2, 5 and 8 while echo 3, 6, and 9 were recorded after the third excitation. A simulated heart rate of 60 bpm was used for prospective triggering of the phantom experiments.

Ethics Statement

For the *in vivo* feasibility study, 8 healthy subjects (mean age: 27±3 years, 5 females, mean BMI: 24 kg/m^2, mean heart rate: 78 bpm) without any known history of cardiac disease were included after due approval by the local ethical committee (registration number DE/CA73/5550/09, Landesamt für Arbeitsschutz, Gesundheitsschutz und technische Sicherheit, Berlin,
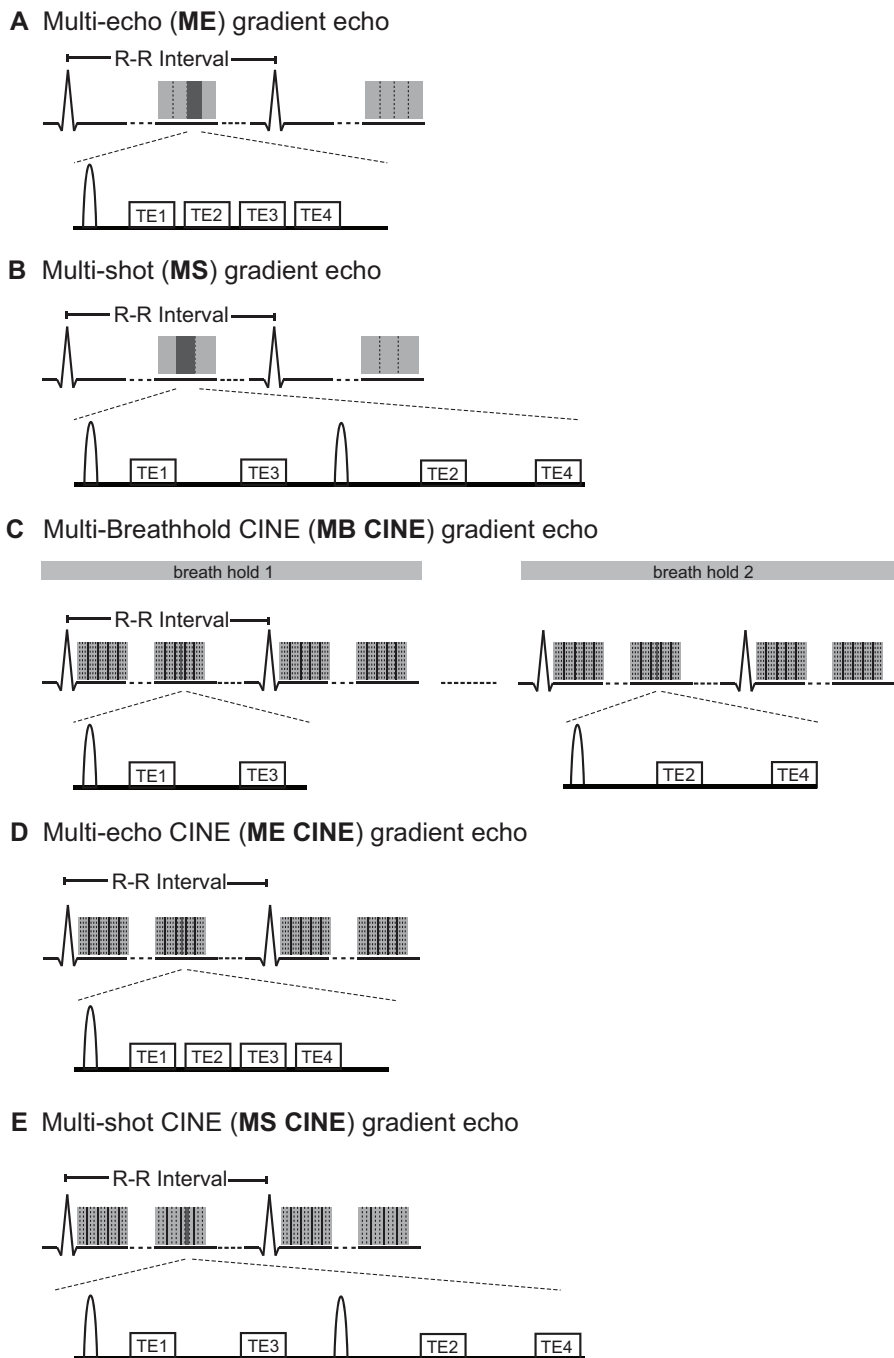
A Multi-echo (**ME**) gradient echo

B Multi-shot (**MS**) gradient echo

C Multi-Breathhold CINE (**MB CINE**) gradient echo

D Multi-echo CINE (**ME CINE**) gradient echo

E Multi-shot CINE (**MS CINE**) gradient echo

Figure 1. Synopsis of multi-echo gradient echo strategies used for T$_2^*$ mapping at 7.0 T. A). Conventional multi-echo (**ME**) gradient echo for single cardiac phase myocardial T$_2^*$ mapping. Multiple echoes are acquired after excitation to obtain a set of T$_2^*$ weighted images. The competing constraints of inter echo time and spatial resolution inherent to the **ME** approach are addressed by the **B**) interleaved multi-shot multi-echo (**MS**) gradient echo technique. In **MS** a set of excitations is employed together with echo interleaving echoes to acquire a set of T$_2^*$ weighted images. **C**) The multi-breath-hold multi-echo (**MB CINE**) gradient echo technique allows myocardial CINE T$_2^*$ mapping by interleaving the echoes over several breath-holds. For benchmarking **D**) multi-echo CINE (**ME CINE**) gradient echo and **E**) multi-shot multi-echo CINE (**MS CINE**) were applied for T$_2^*$ mapping in phantom studies. To guide the eye vertical dashed lines refer to k-space lines. Vertical solid lines refer to cardiac phases. A unipolar readout using gradient flyback was applied for all strategies.
doi:10.1371/journal.pone.0052324.g001

Germany). Informed written consent was obtained from each volunteer prior to the study.

Volunteer Studies

For each volunteer, slice positioning was carried out following international consensus by the same technician to omit inter-operator variability. Myocardial T$_2^*$ mapping was conducted using the **MS** and the **MB CINE** imaging strategies for all

Table 1. Synopsis of scan time duration and temporal resolution used for the single cardiac phase and CINE T$_2$* mapping protocols.

	ME	MS	MB CINE	ME CINE	MS CINE
scan duration phantom study	25s	49s	3×81s	121s	241s
scan duration *in vivo* **study**	-	24s	3×22s	-	-
acquisition window length	205ms	192ms	36ms	38ms	36ms

The scan duration of **MS** protocols is doubled versus **ME** protocols. For *in vivo* T$_2$* mapping **MS** and **MB CINE** were applied. CINE protocols provided an acquisition window length of about 36 ms, which renders the impact of cardiac motion effects rather low. The acquisition window length is given by the number of k-spaces lines acquired per cardiac cycle times the repetition time.
doi:10.1371/journal.pone.0052324.t001

subjects. For this purpose, a mid-ventricular short axis view and a four chamber view were used. Imaging parameters were set to: acquisition data matrix = 256×224, FOV = (288×252) mm^2, in-plane resolution = (1.1×1.1) mm^2, slice thickness = 4 mm if not otherwise stated. A nominal flip angle of $\alpha = 20°$ has been applied; and electro magnetic field (EMF) simulations using the human voxel model "Duke" were conducted for transmission field shaping to enhance B$_1^+$ uniformity across the heart [36,37,41]. Echo times ranging from 2.04 ms to 10.20 ms were applied. Three

excitations together with 3 echoes per excitation were used to ensure an inter-echo time of 1.02 ms. With the first excitation, echo 1, 4 and 7, were acquired. The second excitation covered echo 2, 5 and 8. Echo 3, 6, and 9 were recorded after the third excitation. Moderate acceleration (R = 2 for **MS** and R = 3 for **MB CINE**) in conjunction with GRAPPA reconstruction [42] was applied to reduce the breath-hold time. For single cardiac phase acquisitions, the **MS** protocol was prospectively triggered to place data acquisition at end-diastole or end-systole. For prospectively triggered CINE T$_2$* mapping, 25 cardiac phases were acquired for a heart rate of 60 bpm. Phase images of the first two echoes (TE$_1$ = 2.04 ms, TE$_2$ = 3.06 ms) of **MS** were used to determine B$_0$ field maps offline.

Prior to T$_2$* mapping, volume selective B$_0$ shimming was conducted to reduce static magnetic field inhomogeneities [43,44]. In doing so, the susceptibility weighting will be dictated by microscopic B$_0$ susceptibility gradients, rather than by macroscopic B$_0$ field inhomogeneities. For this purpose, a 2D multi-slice, cardiac gated, breath-hold double echo (**DE**) gradient echo sequence (TE$_1$ = 3.06 ms, TE$_2$ = 5.10 ms) was used for B$_0$ field mapping. Cardiac gating and breath-holding were applied to reduce and possibly eliminate phase contributions induced by cardiac and respiratory motion. The shim volume was adjusted to cover the left and right ventricle in the four chamber view and in the short axis view of the heart. Data acquisition for B$_0$ shimming was adjusted to diastole. This choice is based on previous reports which demonstrated that field maps showed a negligible temporal variation across the cardiac cycle [43]. For the shim volumes, linear and second order room temperature shims were calculated to reduce the frequency shift across the phantom or across the

Table 2. Survey of T$_2$* derived from phantom studies for single cardiac phase and for CINE T$_2$* mapping techniques.

Slice thickness	Mapping technique				
	ME mean±std	MS mean±std	MB CINE mean±std (temporal std)	ME CINE mean±std (temporal std)	MS CINE mean±std (temporal std)
[mm]	[ms]	[ms]	[ms]	[ms]	[ms]
8	26.1±3.7	26.7±3.0	28.3±2.8	26.9±3.2	27.2±2.6
			(0.4)	(0.4)	(0.3)
	18.3±0.8	18.6±0.8	19.5±0.9	18.6±0.7	19.3±0.7
			(0.3)	(0.1)	(0.3)
6	27.5±2.5	27.2±1.8	28.5±1.9	27.9±2.3	27.6±1.7
			(0.4)	(0.5)	(0.4)
	19.0±0.6	19.2±0.7	19.7±0.7	19.2±0.6	19.5±0.9
			(0.4)	(0.2)	(0.4)
4	28.6±1.6	27.7±1.3	30.2±1.5	29.0±1.5	28.7±1.2
			(0.5)	(0.5)	(0.5)
	19.4±0.7	19.3±0.6	19.8±1.0	19.5±0.8	19.7±1.3
			(0.7)	(0.4)	(0.7)
2.5	30.0±1.3	28.7±1.1	30.7±1.3	30.2±1.3	29.8±1.3
			(0.7)	(0.6)	(0.8)
	19.6±0.9	19.5±2.2	20.1±1.7	19.9±1.3	20.1±2.1
			(1.2)	(0.6)	(1.2)

Mean T$_2$* and standard deviation of T$_2$* derived from **ME, MS, ME CINE, MS CINE** and **MB CINE** acquisitions using a slice thickness ranging from 8 mm to 2.5 mm. For all slice thicknesses the top rows show T$_2$* for the long T$_2$* phantom while the bottom rows show T$_2$* for the medium T$_2$* phantom. For the long T$_2$* phantom T$_2$* was observed for a ROI (diameter 2 cm) placed in the iso-center of an axial slice of the phantom. For the mediumT$_2$* phantom T$_2$* was observed for a ROI (diameter 6 cm). Please note, for CINE protocols temporal T$_2$* variation is given in parentheses as standard deviation of mean T$_2$* over the CINE cycle.
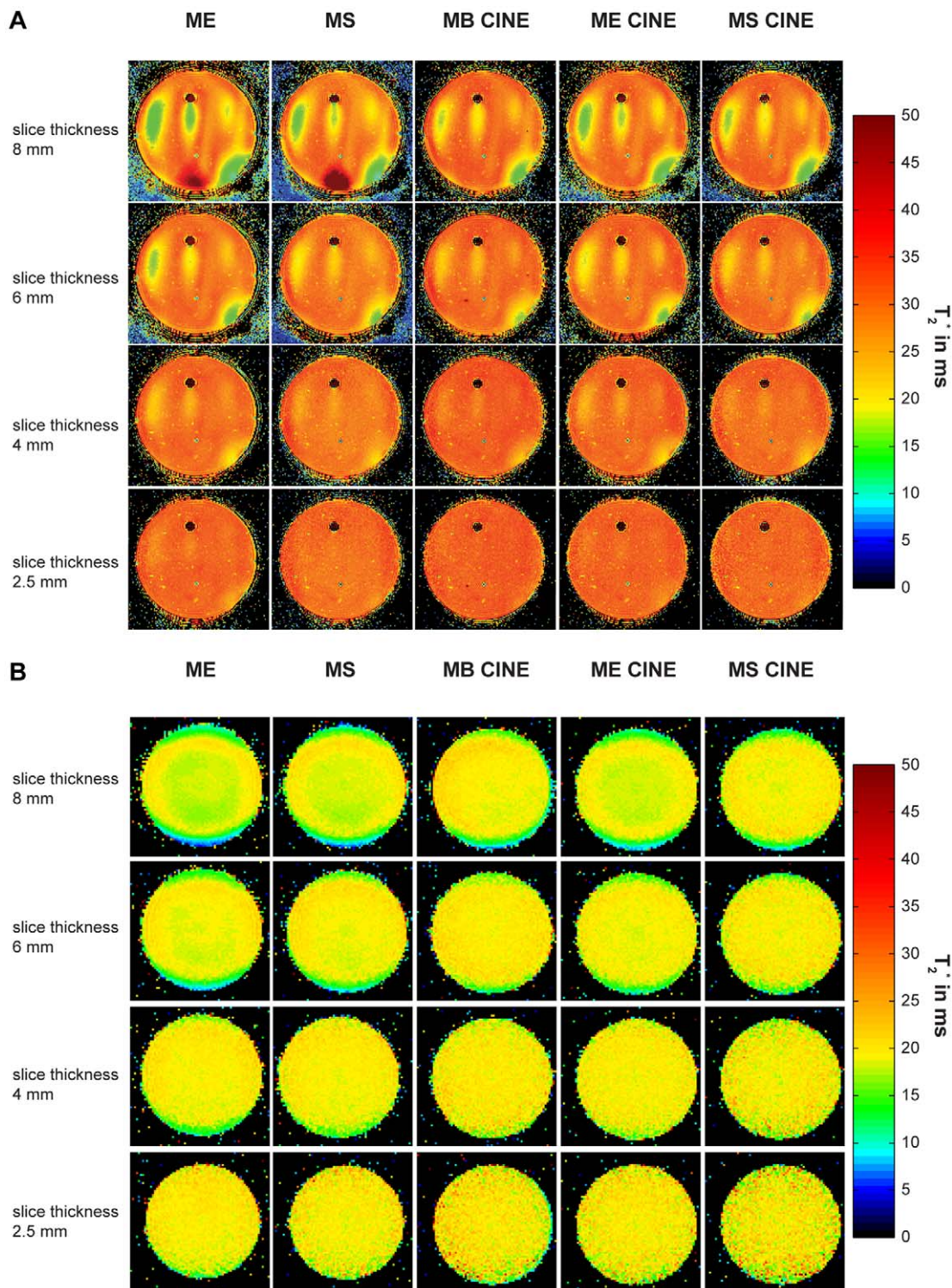doi:10.1371/journal.pone.0052324.t002

Figure 2. Survey of T$_2$* maps derived from phantom studies. T$_2$* maps obtained for all imaging strategies using a long T$_2$* (**A**) and a medium T$_2$* phantom (**B**). Slice thicknesses ranging from 8 mm to 2.5 mm (top to bottom) were applied. T$_2$* analysis revealed similar results for all T$_2$* mapping strategies. For a slice thickness of 8 mm T$_2$* varied substantially across both phantoms. The uniformity in T$_2$* was improved for a slice thickness of 6 mm and even further enhanced for a slice thickness of 4 mm or 2.5 mm.
doi:10.1371/journal.pone.0052324.g002

heart with the goal to render B$_0$ uniform. The overall protocol time, including localizer, slice angulation, volume selective B$_0$ mapping routine, 2D FLASH CINE imaging (4 chamber view and short axis view) and T$_2$* mapping using MS and MB CINE

was approximately 30 minutes. Table 1 outlines the breath hold times used for MS and MB CINE T$_2$* mapping in healthy volunteers.
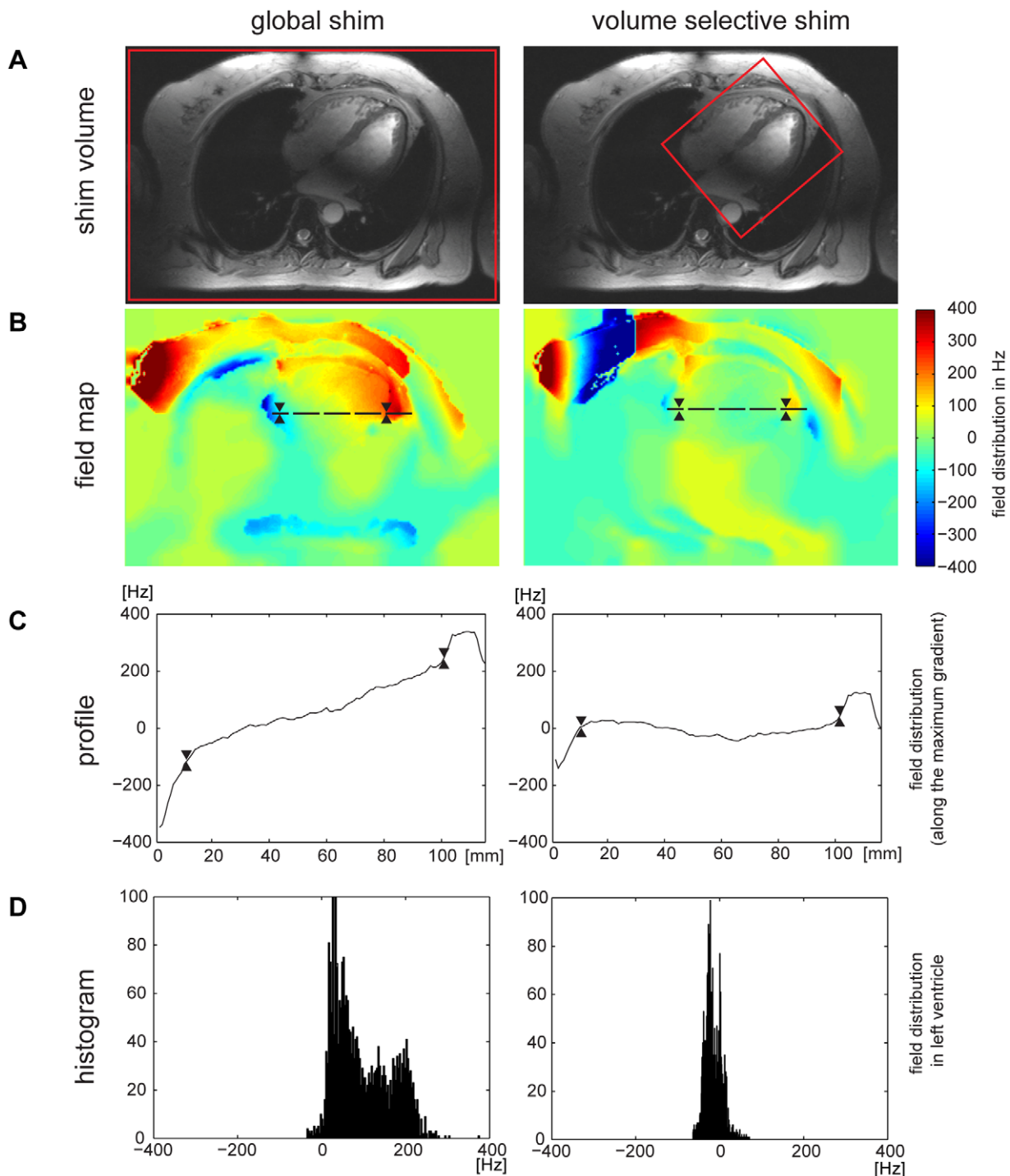
Figure 3. B$_0$ distribution for global and volume selective B$_0$ shimming of a four chamber view of the heart. A) Four chamber view of the heart illustrating the positioning of the volume (marked in red) used for global (left) and volume selective (right) shimming. **B**) B$_0$ field variation derived from global and volume selective shimming. For this subject the global shim provided a peak-to-peak field variation of about 400 Hz across the entire heart. After volume selective shimming peak-to-peak B$_0$ variation across the heart was reduced to approximately 80 Hz. The direction of the maximal B$_0$ gradient is illustrated by the dashed black line in **B**) and the corresponding profile of B$_0$ field distribution is plotted in **C**). To guide the eye the epicardial borders are marked in **B**) and **C**) by two triangles. The histogram of the field distribution over the left ventricle is shown in **D**). The full width at half maximum is approximately 200 Hz for the globally shimmed B$_0$ field map and was reduced to about 80 Hz after volume selective shimming.

doi:10.1371/journal.pone.0052324.g003
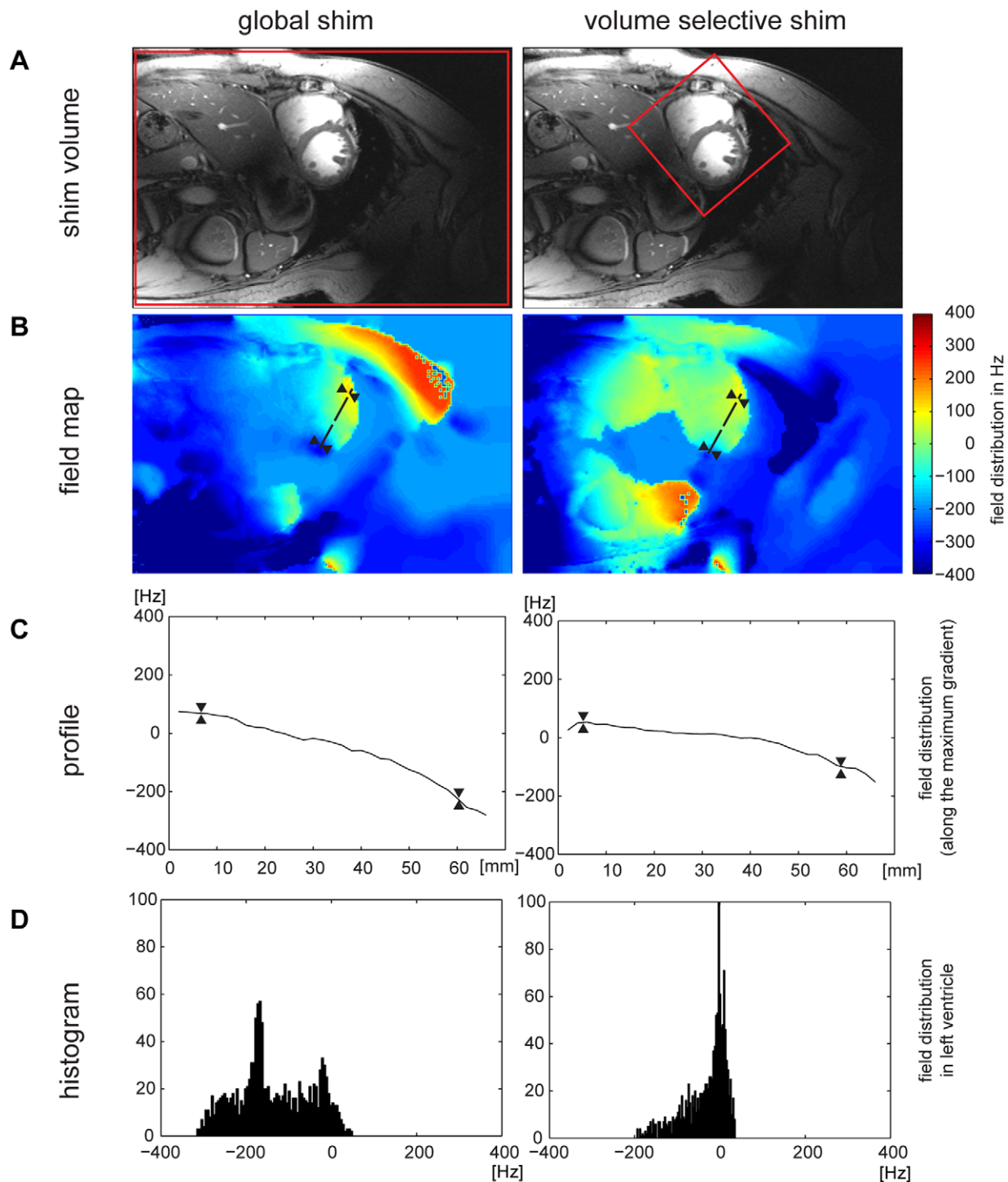
global shim

volume selective shim

Figure 4. B$_0$ distribution for global and volume selective shimming of a mid-ventricular short axis view of the heart. A) Mid-ventricular short axis view of the heart illustrating the positioning of the volume (marked in red) used for volume selective shimming. **B)** B$_0$ field maps. **C)** B$_0$ profile along the direction of the strongest B$_0$ gradient which is highlighted by the dashed black line in **B**). To guide the eye the epicardial borders are marked in **B)** and **C)** by two triangles. **D)** Frequency histogram across the left ventricle. After volume selective shimming a strong susceptibility gradient at the inferior region of the heart could be reduced. The full width at half maximum is approximately 300 Hz for the globally shimmed field map and was reduced to about 80 Hz after volume selective shimming.
doi:10.1371/journal.pone.0052324.g004

Post-Processing and Image Analysis

Image datasets were transferred to a MATLAB (The Mathworks, Natick, USA) workstation and processed offline. For all datasets, T$_2$* was estimated based on a linear equation set obtained from the logarithm of Equation 1, where S$_{(0)}$ was estimated through S$_{(TEmin)}$. The T$_2$* and S$_0$ estimation was used as initialization values to fit the data points to a mono exponential
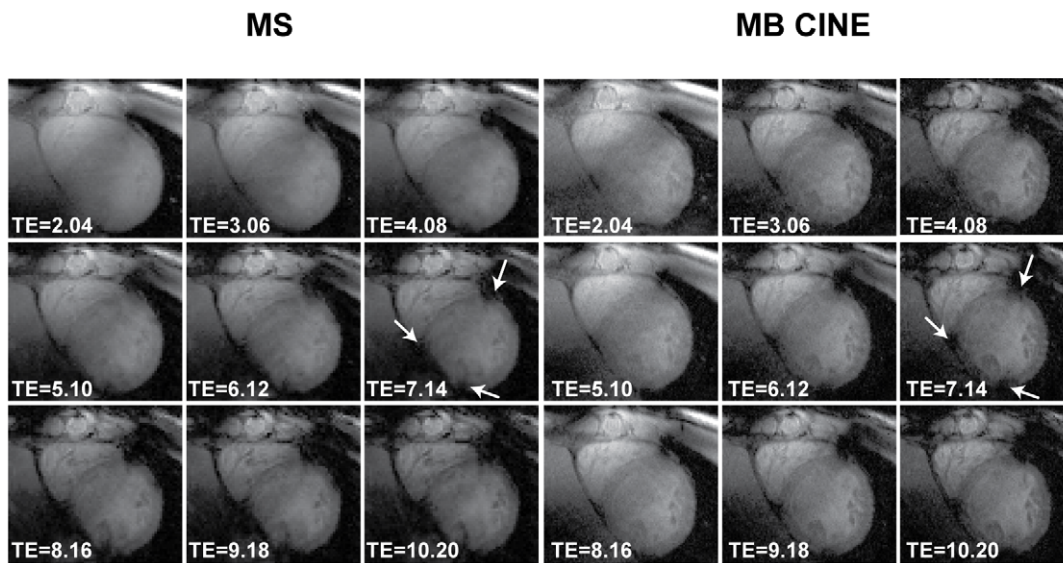
Figure 5. Short axis views derived from single cardiac phase and dynamic CINE T$_2^*$ weighted imaging of the heart. Echo times ranging from 2.04 ms to 10.20 ms were used for **MS** and **MB CINE** acquisitions. A low nominal flip angle of 20° was used to preserve myocardial signal. Image quality observed for **MS** and **MB CINE** acquisitions is comparable. No severe susceptibility artifacts were detected in the septum and in the lateral wall for TEs ranging between 2.04 ms to 10.20 ms. For anterior and inferior myocardial areas encompassing major cardiac veins susceptibility weighting related signal void was observed for TE >7 ms as highlighted by white arrows.
doi:10.1371/journal.pone.0052324.g005

decay (Equation 1) based on the MATLAB region trust algorithm.

$$S_{(TE)} = S_0 * e^{\frac{-TE}{T2^*}} \qquad (1)$$

For T$_2^*$ assessment of the phantom data, a ROI covering the entire central axial view of the phantom was used. Average and standard deviation of T$_2^*$ were determined.

For examination of the *in vivo* data, an affine registration of the **MB CINE** datasets was incorporated into the post-processing procedure to compensate for misalignments due to the use of multiple breath-hold periods. The affine registration is landmark based. It shifts and shears the datasets derived from multiple breath-held acquisitions. Landmarks were set manually. Mid-ventricular short axis T$_2^*$ maps were segmented according to the standardized myocardial segmentation and nomenclature for tomographic imaging of the heart [45]. For each segment of the
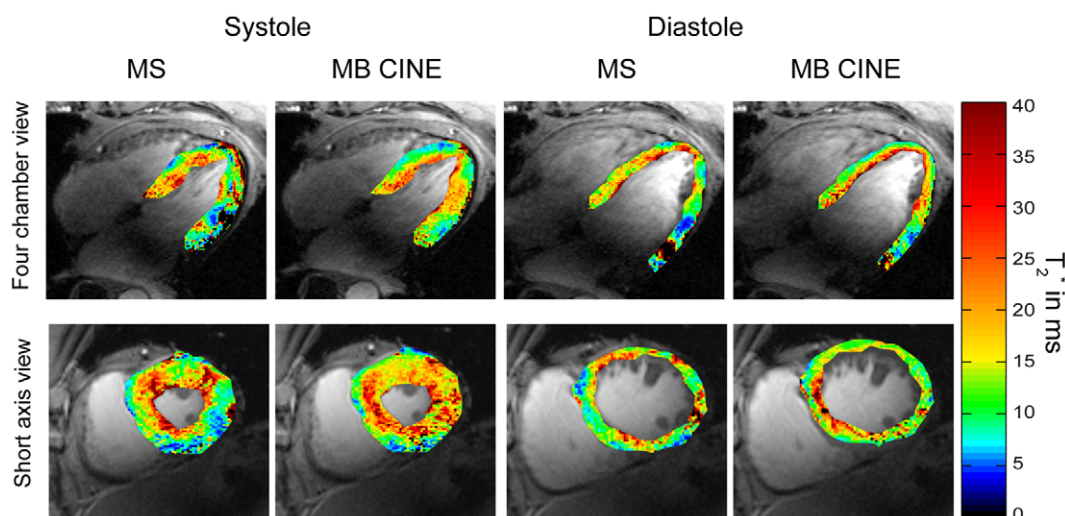

Figure 6. T$_2^*$ maps derived from single cardiac phase and dynamic CINE mapping of a four chamber and short axis view of the heart at end-diastole and end-systole. Four chamber (top) and short axis view T$_2^*$ colour maps obtained from **MS** and **MB CINE** superimposed to anatomical 2D CINE FLASH gray scale images. For **MB CINE** a systolic and diastolic phase was chosen to match the cardiac phase with the end-systolic and end-diastolic phase derived from **MS**. T$_2^*$ maps deduced from **MS** and **MB CINE** showed no significant differences between both methods in the segmental analysis of T$_2^*$ values. When comparing systolic and diastolic T$_2^*$ maps significant differences were found with p = 0.002 for MS and p = 0.01 for **MB CINE**.
doi:10.1371/journal.pone.0052324.g006

Table 3. Summary of mean and standard deviation of T$_2$* (in ms) at end-diastole and at end-systole.

	cardiac segment					
	7	**8**	**9**	**10**	**11**	**12**
MB CINE end-systole	13.7±2.9	17.4±2.5	14.8±1.8	10.5±4.2	8.3±2.4	10.9±1.7
MB CINE end-diastole	16.8±2.2	17.3±1.4	16.3±2.2	12.0±3.6	11.4±2.8	12.5±1.9
MS end-systole	12.4±2.1	17.2±2.7	15.7±2.9	7.6±2.1	10.2±2.0	13.6±1.9
MS end-diastole	14.0±1.8	17.2±2.6	16.5±2.0	10.6±4.4	11.4±2.5	15.7±2.0

Mean T$_2$* (in ms) averaged over all subjects for each cardiac segment of a mid-ventricular short axis derived from single cardiac phase **MS** and from **MB CINE** acquisitions at end-diastole and at end-systole. T$_2$* values obtained for both approaches show a fair agreement. The statistical analysis showed no significant difference between T$_2$* derived from **MS** and T$_2$* deduced from **MB CINE** acquisitions.
doi:10.1371/journal.pone.0052324.t003

mid-ventricular slice (segment 7–12 according to [45]), T$_2$* values were calculated during end-diastole and end-systole for the single cardiac phase approach. For assessment of temporal changes in T$_2$* throughout the cardiac cycle ROIs encompassing segment 7 to 12 were defined and analysed for all cardiac phases derived from MB CINE. For this purpose, the position and shape of the ROI was carefully adjusted throughout the cardiac cycle to account for myocardial contraction and relaxation. Also, this approach was used to include only compact myocardium into the analysis so that blood or trabecular tissue contributions can be eliminated. For careful delineation of the myocardial borders 2D CINE FLASH (flip angle = 32°, acquisition data matrix = 256×224, FOV = (288×252) mm^2, in-plane resolution = (1.1×1.1) mm^2, slice thickness = 4 mm, TE = 2.8 ms, TR = 4.2 ms) was used. Mean values and standard deviation of T$_2$* were calculated for all ROIs. Statistical analysis was performed to test for data distribution and group differences using R project for statistical computing (OpenSource: www.r-project.org). A p-value below 0.05 was considered as statistically significant.

Results

Phantom Studies

T$_2$* maps derived with all imaging strategies for the phantom experiments are surveyed in Figure 2 and Table 2 and show that all imaging strategies provide similar T$_2$* maps. For the long T$_2$* phantom, T$_2$* varied from 13.6 ms to 37.4 ms across the entire central axial slice when using a slice thickness of 8 mm. The non-uniformity in T$_2$* was reduced for 6 mm slices with T$_2$* ranging
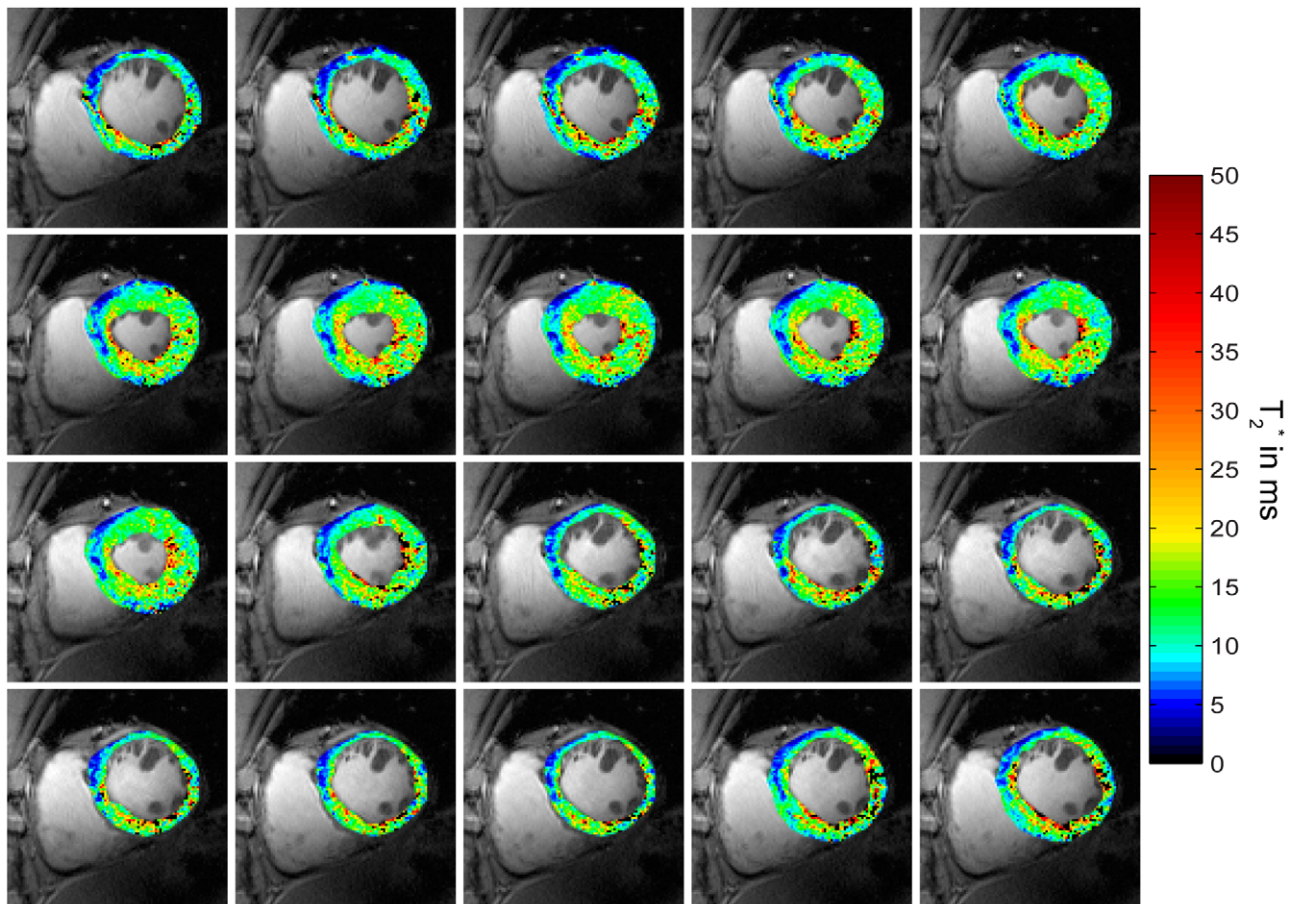

Figure 7. CINE T$_2$* maps over the cardiac cycle. Short axis view T$_2$* colour maps derived from **MB CINE** acquisitions across the cardiac cycle overlaid to conventional 2D CINE FLASH images. T$_2$* values are increasing from diastole to systole, especially for endocardial layers. Macroscopic susceptibility induced T$_2$* reduction effects were present at the epicardium at inferior regions.
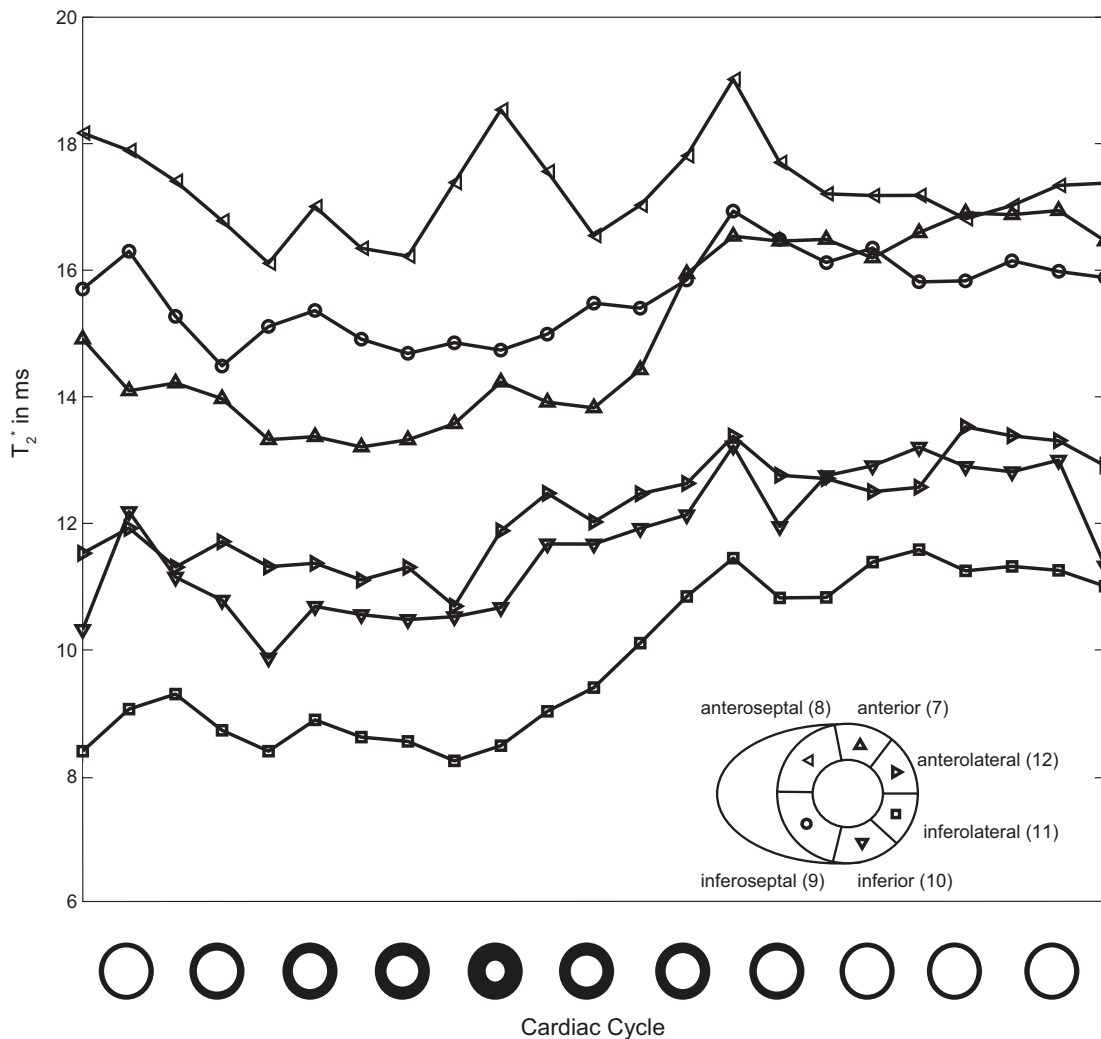doi:10.1371/journal.pone.0052324.g007

Figure 8. Analysis of T$_2$* across the cardiac cycle. Synopsis of the evolution of mean T$_2$* averaged over all subjects for standard mid-ventricular segments of the heart. T$_2$* derived from each cardiac segment are plotted versus the cardiac cycle. T$_2$* changes over the cardiac cycle. Averaging T$_2$* over all mid-ventricular myocardial segments revealed that T$_2$* increases approximately 27% between systole and diastole. Myocardial T$_2$* was derived from **MB CINE** acquisitions. Prospective triggering was used which resulted in a gap at end-diastole of approximately 100 ms depending on the heart rate. For this reason the cardiac cycle is normalized for all subjects without including this gap.
doi:10.1371/journal.pone.0052324.g008

from 19.7 ms to 33.9 ms across the entire central axial slice. T$_2$* non-uniformity across the central axial slice was further reduced upon further reducing the slice thickness to 4 mm and 2.5 mm, which showed T$_2$* of (29.1±1.5) ms and (29.9±1.7) ms, respectively. T$_2$* values derived from a ROI (d = 2 cm) placed in the iso-center of the central axial slice of the phantom varied between 26.1 ms (**ME**) and 28.3 ms (**MB CINE**) for a slice thickness of 8 mm. In comparison, T$_2$* values ranging from 28.7 ms (**MS**) to 30.7 (**MB CINE**) were observed for the same small ROI when using a slice thickness of 2.5 mm. T$_2$* values derived from CINE imaging remained constant (std <1 ms) throughout the cycle given by the gating paradigm.

For the medium T$_2$* phantom, mean T$_2$* varied between 18.3 ms and 19.3 ms for a ROI covering the entire central axial slice (slice thickness = 8 mm). For a slice thickness of 6 mm, mean T$_2$* values were ranging from 19.0 ms to 19.9 ms. T$_2$* mapping using a slice thickness of 4 mm yielded mean T$_2$* values ranging from 19.3 ms to 19.8 ms. For a 2.5 mm slice thickness the range of mean T$_2$* values encompassed 19.5 ms to 20.1 ms. For this slice thickness the standard deviation of T$_2$* across the central slice of the phantom was approximately 2 ms for **MS, MB and MS CINE** due to SNR constraints. T$_2$* values derived from CINE imaging remained constant (std <1 ms) throughout the cycle given by the cardiac gating paradigm.

In all phantom experiments, the acquisition time of the **MS** approach was doubled versus the **ME** approach, as summarized in Table 1. In **MS,** only 5 views per segment were recorded while **ME** used 10 views per segment. This approach has been deliberately chosen already at this stage to ensure that the acquisition windows do not exceed the cardiac rest period in the *in vivo* studies. For **ME CINE,** only two views per segment were used to accomplish an acquisition window of 38 ms which increased the total scan duration to 121 s in the phantom studies. This scan duration was doubled for **MS CINE** since only one view per segment could be used for this approach.
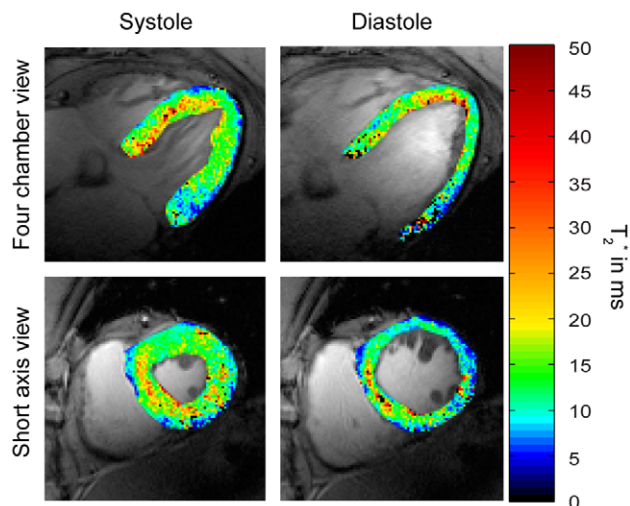
Figure 9. High spatial resolution four chamber and short axis view T$_2^*$ maps derived from T2* weighted CINE imaging. For **MB CINE** slice thickness was reduced to 2.5 mm while maintaining the in-plane spatial resolution of (1.1×1.1) mm^2. Compared to the results obtained with **MB CINE** using a slice thickness of 4 mm, changes in T$_2^*$ from epicardial to endocardial septal myocardial layers are more pronounced, in particular during systole.
doi:10.1371/journal.pone.0052324.g009

Volunteer Studies

For the *in vivo* studies, **MS** and **MB CINE** were applied using a slice thickness of 4 mm to balance the competing constraints between SNR and B$_0$ background gradients. A reduction in slice thickness helps to reduce intra-voxel dephasing due to B$_0$ gradients along the slice direction. This slice thickness is afforded by the SNR advantage inherent to 7.0 T and is smaller than that commonly used for T$_2^*$ mapping at 1.5 T and 3.0 T. Localized shimming was performed to reduce static magnetic field inhomogeneities to make sure that the susceptibility weighting is not dominated by macroscopic B$_0$ field inhomogeneities but rather by microscopic B$_0$ susceptibility gradients. Figure 3 and Figure 4 depict B$_0$ maps together with B$_0$ profiles across the heart and frequency histograms of the heart obtained prior to and after volume selective shimming for a four chamber (Figure 3) and short axis view (Figure 4). The B$_0$ field maps following global shimming showed a mean peak-to-peak field difference of approximately 400 Hz across the heart for a four chamber view (Figure 3B) and approximately 300 Hz for a mid-ventricular short axis view (Figure 4B). After volume selective shimming, a mean peak-to-peak B$_0$ difference of approximately 80 Hz was found across the entire heart for a four chamber view (Figure 3B) and a mid-ventricular short axis view (Figure 4B) of the heart. For the left ventricle a B$_0$ peak-to-peak difference of approximately 65 Hz was observed after volume selective shimming. For both short axis view and 4 chamber view, a maximum in-plane field gradient of approximately 20 Hz/mm (through-plane approximately 80 Hz/voxel for a 4 mm slice thickness) was observed at the epicardial fat/lung interface of the inferior and inferolateral segment as indicated by the B$_0$ maps and frequency profiles shown in Figure 3B,C and Figure 4B,C. This local B$_0$ gradient translates into a phase loss of approximately 80% at the maximum echo time of TE = 10 ms. However, the through-plane field gradient at the epicardium/lung interface is much more pronounced versus the through-plane field gradient obtained for the left and right ventricle, as demonstrated in Figure 3B/C. For myocardial

anterior, anterolateral and inferoseptal segments a mean in-plane B$_0$ gradient of approximately 3 Hz/mm was obtained which translates into an through-plane B$_0$ dispersion of approximately 12 Hz/voxel for a 4 mm slice thickness. This B$_0$ gradient implies that macroscopic intravoxel dephasing effects are of minor effect for the TE range used. Inspite of B$_1^+$ shaping using EMF simulations the signal intensity change across the myocardium of a mid-ventricular short axis slice was found to be approximately 40%.

We next employed **MS** and **MB CINE** to determine the limits of susceptibility artifacts. Figure 5 shows end-diastolic short axis views derived from **MS** and **MB CINE** acquisitions using echo times ranging from 2.04 ms to 10.20 ms. With the flip angle of 20°, RF power deposition was well in the SAR limits given by the IEC guidelines [46], which were confirmed by rigorous electromagnetic field simulations [36,37]. The low flip angle was deliberately chosen to preserve myocardial signal by reducing T$_1$-saturation effects. Although this approach results in a low contrast between the blood pool and the surrounding myocardium (Figure 5), it is beneficial for myocardial T$_2^*$ quantification. Unlike previous reports at 1.5 T and 3.0 T double inversion recovery prepared blood suppression was not used since this approach does not meet the requirements of CINE T$_2^*$ mapping. It should be noted that no differences in mean T$_2^*$ values were found for black blood versus white blood acquisitions at 1.5 T [47]. No severe susceptibility artifacts were detected in the septum (segment 8–9) and in the lateral wall (segment 11–12) for TEs ranging between 2.04 ms to 10.20 ms. For anterior (segment 7) and inferior (segment 10) myocardial areas, which encompass major cardiac veins, a signal void related to the susceptibility weighting was observed for TE >7 ms (Figure 5).

We next explored myocardial T$_2^*$ using single cardiac phase (**MS**) and dynamic CINE (**MB CINE**) acquisitions. Figure 6 shows end-systolic and end-diastolic short axis and four chamber view T$_2^*$ maps. Regions of T$_2^*$ reduction were observed in areas adjacent to the large cardiac vein and the posterior vein. A paired t-test showed no significant differences in T$_2^*$ values observed for **MS** and **MB CINE** strategies. (p = 0.8 for diastole, p = 0.7 for systole). The differences between the **MS** the **MB CINE** imaging strategy including all mid-ventricular segments were found to be T$_2^*_{diff}$ = (0.2±3.7) ms at end-diastole and T$_2^*_{diff}$ = (−0.2±3.4) ms at end-systole. **MS** and **MB CINE** showed a mean T$_2^*$ of approximately 14 ms for mid-ventricular myocardium. Regional T$_2^*$ variation was observed for mid-ventricular myocardium. The longest T$_2^*$ values were found for segment 8 (**MS:** T$_2^*$ = 17.2 ms, **MB CINE:** T$_2^*$ = 17.3 ms), segment 9 (**MS:** T$_2^*$ = 16.5, **MB CINE:** T$_2^*$ = 16.3) and segment 7 (**MS:** T$_2^*$ = 14.0 ms, **MB CINE:** T$_2^*$ = 16.8 ms). For segment 10 and segment 11 lower T$_2^*$ values were observed (segment 10: **MS:** T$_2^*$ = 10.6 ms, **MB CINE:** T$_2^*$ = 12.0 ms, segment 11: **MS:** T$_2^*$ = 11.4 ms, **MB CINE:** T$_2^*$ = 11.4 ms). A synopsis of T$_2^*$ values averaged over all subjects for **MS** and **MB CINE** acquisitions at end-diastole is given in Table 3.

A closer examination revealed a significant difference between myocardial T$_2^*$ obtained at end-diastole and those derived from end-systolic acquisitions. Indeed, an increase in T$_2^*$ can be clearly observed, particularly at the septum, during systolic phases (Figure 6, Figure 7). Figure 7 shows exemplary CINE T$_2^*$ maps for all phases of the cardiac cycle and illustrates the changes of T$_2^*$ over the cardiac cycle. A paired t-test comparing end-diastolic and end-systolic phase T$_2^*$ values for all segments revealed p = 0.002 for single cardiac phase **MS** acquisitions and p = 0.01 for **MB CINE** acquisitions. When averaging the T$_2^*$ time course from all subjects an increase in T$_2^*$ of 27%±6% in all cardiac segments

could be observed over the cardiac cycle (Figure 8). The shortest T$_2$* values were noted for a cardiac phase placed in systole. For all cardiac segments, the longest T$_2$* values were found after the onset of diastole. The largest T$_2$* increase over the cardiac cycle was found for segment 7 (ΔT$_2$* = +3.7 ms) and segment 10 (ΔT$_2$* = +3.4 ms).

To demonstrate the baseline SNR advantage of 7.0 T and to further reduce intravoxel dephasing along the slice direction, the slice thickness was reduced to 2.5 mm while maintaining the in-plane spatial resolution of (1.1×1.1) mm^2 in the **MB** CINE protocol. Figure 9 shows short axis and four chamber view T$_2$* maps, which demonstrate the high spatial resolution. This approach further manifests the observed changes in T$_2$* during systole and diastole and also indicates the high sensitivity of susceptibility mapping by visualizing differences in T$_2$* between endocardial and epicardial layers of the myocardium.

Discussion

This work shows the feasibility of high spatially and temporally resolved myocardial T$_2$* mapping at 7.0 T. For this purpose T$_2$* weighted, gradient echo based imaging techniques using single cardiac phase (**MS**) and CINE (**MB CINE**) acquisition regimes were benchmarked against T$_2$* mapping techniques commonly used in current clinical practice at 1.5 T and 3.0 T. These two imaging techniques were first examined in detail in phantom experiments.

It might be considered as a remaining limitation that our results might be affected by residual macroscopic B$_0$ gradients. However, our B$_0$ mapping results suggest that a reasonable B$_0$ uniformity across the heart and the left ventricle can be achieved at 7.0 T which is embodied by a mean through-plane gradient of 3 Hz/mm across the left ventricle. In this regard it should be also noted that our measurements of the B$_0$ field distribution after volume selective shimming of our uniform phantom provided a through slice peak-to-peak B$_0$ variation of 80 Hz along a distance of 4 cm which translates into 2 Hz/mm. This B$_0$ field gradient is similar to what has been observed for the left and right ventricle which showed a mean of 3 Hz/mm.

The frequency shift across the heart reported here compares well with previous 3.0 T studies which reported a peak-to-peak off-resonance variation of (262±58) Hz over the left ventricle and the right ventricle (basal short axis view) for a global shim [48]. This B$_0$ inhomogeneity was improved to (176±30) Hz and (121±31) Hz with the use of localized linear and second-order shimming [48]. The use of an enhanced locally optimized shim algorithm, which is tailored to the geometry of the heart, afforded a reduction of the peak-to-peak frequency variation over the heart from 235 Hz to 86 Hz at 3.0 T [49]. Another pioneering study showed a peak-to-peak off-resonance of (71±14) Hz for short axis views acquired at 1.5 T [40] using global shimming.

Previous reports on brain imaging/spectroscopy suggest that third-order and even higher order shims help to further enhance B$_0$ uniformity across the target anatomy [50,51]. For this purpose extra shim drum inserts are retrofitted to the scanner. Notwithstanding its utility the current implementation limits the available space inside of the MR scanner bore which would be prohibitive for cardiac or body MRI at 7.0 T. Other attempts to integrate third order shim coils into high performance 7.0 T whole body gradient coil designs were found to show pronounced gradient non-linearity for spherical volumes with a diameter larger than (20–25) cm; a behavior which does not meet the requirements of cardiac or body MR. Obviously, another approach to further reduce the residual impact of through-plane gradients and intra-

voxel dephasing B$_0$ gradients is the use of even thinner slices and the reduction in voxel size. To meet this goal we pushed the envelope by using a slice thickness as thin as 2.5 mm together with an in-plane resolution of (1.1×1.1) mm^2. This slice thickness and in-plane resolution is afforded by the SNR advantage inherent to 7.0 T. The corresponding voxel size is by a factor of five smaller than commonly used for T$_2$* mapping at 1.5 T and 3.0 T. However, it should be noted that the move to even thinner slices and smaller voxel sizes – ideally one might opt to use an infinitesimal small voxel – would disturb the balance dictated by the competing constraints of SNR and background gradients effects.

This study sheds further light to the current literature since it demonstrates the applicability of **MS** and **MB CINE** for T$_2$* mapping of normal myocardium at 7.0 T. While we recognize a limitation due to the limited number of healthy subjects studied, we believe this feasibility study to be an essential precursor to a larger 7.0 T study involving healthy and patient cohorts. Such a study would aid to establish the lower limits for normal myocardial T$_2$* values versus the clinically established normal values for T$_2$* of healthy myocardium at 1.5 T and 3.0 T. To this end, T$_2$* mapping at 7.0 T may be useful to extend the capabilities and the dynamic range of the sensitivity of the established approach used for quantification of myocardial iron content. With this in mind, we anticipate to extend our efforts towards clinical studies at 7.0 T including thalassemia major patients, whose T$_2$* relaxation times will be benchmarked against the normal values of healthy subjects.

Our results show that T$_2$* obtained for human myocardial muscle tissue at 7.0 T ranges from 9 ms to 18 ms. This is in line with T$_2$* = (15.8±0.2) ms recently observed for hind limb skeletal muscle in rats at 7 Tesla [52] Admittedly, the absolute spatial resolution demonstrated for T$_2$* mapping of the human heart at 7.0 T is still by an order of magnitude below that previously reported for *ex vivo* MR microscopy based T$_2$*mapping of the isolated rat heart [7], which demonstrated that T$_2$*mapping provides an insight into the complex architecture of the heart musculature. However, the effective anatomical spatial resolution – voxel size per anatomy – is getting close to what has been demonstrated for animal models. This improvement might be beneficial to gain a better insight into the myocardial microstructure *in vivo* with the ultimate goal to visualize myocardial fibers or to examine helical angulation of myocardial fibers using T$_2$* mapping, since the susceptibility effects depend on the tilt angle between blood filled capillaries and the external magnetic field [53]. Myocardial fibre tracking using T$_2$* mapping holds the promise to be less sensitive to bulk motion than diffusion-weighted MR of the myocardium [54,55]. Our results also suggest that the increased susceptibility contrast available at 7.0 T could be exploited to quantitatively study iron accumulations in organs other than the heart with high sensitivity and temporal and spatial resolution superior to what can be achieved at 1.5 T and 3.0 T.

For normal myocardium a T$_2$* value of approximately 37 ms was found at 1.5 T [23]. At 3.0 T a T$_2$* of approximately 27 ms was observed for normal myocardium [56]. These measurements are usually limited to the septum, which shows the lowest spatial variation in T$_2$* [57]. It is elusive to study temporal changes in T$_2$* at 1.5 and 3.0 T due to scan time constraints which are prohibitive for CINE T$_2$* mapping. Of course, single cardiac phase T2* mapping can be applied to diastole and systole as reported previously [58]. This 1.5 T study with thalassemia patients demonstrated mean T$_2$* values of (26.4±14.2) ms for early systole and (25.2±13.1) ms for late diastole, which were found to be not significantly different (P = 0.27). However, the limited T$_2$*

sensitivity together with the temporal resolution used in the study presents a challenge for tracking temporal changes in T$_2$*. Please also note, that these data exhibit a rather large standard deviation of approximately ±13.0 ms, which presents another challenge for assessment of temporal T$_2$* changes.

A careful literature research revealed that no 1.5 T and 3.0 T T$_2$* mapping study has been reported yet which uses a high spatial resolution accomplished here. We would also like to point out that our study is the first study which affords CINE T$_2$* mapping due to inter echo time shortening at 7.0 T. To this end it is interesting to note that the myocardial BOLD effect has been investigated using SSFP imaging, which is sensitive to changes in the relaxation times T$_2$ and T$_1$. In this regard it has been shown recently that the signal intensity derived from SSFP imaging of the myocardium varies across the cardiac cycle [59]. This study showed a systole-to-diastole T$_2$ ratio of approximately 1.1 for normal myocardium.

The ability to probe for changes in tissue oxygenation using T$_2$* sensitized imaging/mapping offers the potential to address some of the spatial and temporal resolution constraints of conventional first pass perfusion imaging and holds the promise to obviate the need for exogenous contrast agents. Since microscopic susceptibility increases with field strength, thus making the BOLD effect due to (patho)physiology of interest more pronounced, T$_2$* mapping at 7.0 T might be beneficial to address some of the BOLD sensitivity constraints reported for the assessment of regional myocardial oxygenation changes in the presence of coronary artery stenosis [60] or for the characterization of vasodilator-induced changes of myocardial oxygenation at 1.5 T and at 3.0 T [17].

Conclusion

Our results underscore the challenges of myocardial T$_2$* mapping at 7.0 T due to the propensity to macroscopic susceptibility artefacts and T$_2$* shortening, but demonstrate that these issues can be offset by using tailored shimming techniques together with dedicated acquisition schemes.

Acknowledgments

Author Contributions

Conceived and designed the experiments: FH CT JSM TN. Performed the experiments: FH CT TN. Analyzed the data: FH JSM. Contributed reagents/materials/analysis tools: FH SW. Wrote the paper: FH CT SW JSM TN.

References

1. Positano V, Pepe A, Santarelli MF, Scattini B, De Marchi D, et al. (2007) Standardized T2* map of normal human heart in vivo to correct T2* segmental artefacts. NMR Biomed 20: 578–590.
2. He T, Gatehouse PD, Kirk P, Mohiaddin RH, Pennell DJ, et al. (2008) Myocardial T(*)2 measurement in iron-overloaded thalassemia: An ex vivo study to investigate optimal methods of quantification. Magn Reson Med 60: 350–356.
3. Heinrichs U, Utting JF, Frauenrath T, Hezel F, Krombach GA, et al. (2009) Myocardial T2* mapping free of distortion using susceptibility-weighted fast spin-echo imaging: a feasibility study at 1.5 T and 3.0 T. Magn Reson Med 62: 822–828.
4. Hernando D, Vigen KK, Shimakawa A, Reeder SB (2011) R 2* mapping in the presence of macroscopic B(0) field variations. Magn Reson Med.
5. Bauer WR, Nadler W, Bock M, Schad LR, Wacker C, et al. (1999) The relationship between the BOLD-induced T(2) and T(2)(*): a theoretical approach for the vasculature of myocardium. Magn Reson Med 42: 1004–1010.
6. Bauer WR, Nadler W, Bock M, Schad LR, Wacker C, et al. (1999) Theory of the BOLD effect in the capillary region: an analytical approach for the determination of T2 in the capillary network of myocardium. Magn Reson Med 41: 51–62.
7. Köhler S, Hiller KH, Waller C, Jakob PM, Bauer WR, et al. (2003) Visualization of myocardial microstructure using high-resolution T*2 imaging at high magnetic field. Magn Reson Med 49: 371–375.
8. Friedrich MG, Niendorf T, Schulz-Menger J, Gross CM, Dietz R (2003) Blood oxygen level-dependent magnetic resonance imaging in patients with stress-induced angina. Circulation 108: 2219–2223.
9. Manka R, Paetsch I, Schnackenburg B, Gebker R, Fleck E, et al. (2010) BOLD cardiovascular magnetic resonance at 3.0 tesla in myocardial ischemia. J Cardiovasc Magn Reson 12: 54.
10. Jahnke C, Gebker R, Manka R, Schnackenburg B, Fleck E, et al. (2010) Navigator-gated 3D blood oxygen level-dependent CMR at 3.0-T for detection of stress-induced myocardial ischemic reactions. JACC Cardiovasc Imaging 3: 375–384.
11. Karamitsos TD, Leccisotti L, Arnold JR, Recio-Mayoral A, Bhamra-Ariza P, et al. (2010) Relationship between regional myocardial oxygenation and perfusion in patients with coronary artery disease: insights from cardiovascular magnetic resonance and positron emission tomography. Circ Cardiovasc Imaging 3: 32–40.
12. Friedrich MG (2010) Testing for myocardial ischemia: the end of surrogates? JACC Cardiovasc Imaging 3: 385–387.
13. Pennell DJ (2010) To BOLDly go where positron emission tomography has been before. Circ Cardiovasc Imaging 3: 2–4.
14. Tsaftaris SA, Tang R, Zhou X, Li D, Dharmakumar R (2012) Ischemic extent as a biomarker for characterizing severity of coronary artery stenosis with blood oxygen-sensitive MRI. J Magn Reson Imaging 35: 1338–1348.
15. Wacker CM, Bock M, Hartlep AW, Beck G, van Kaick G, et al. (1999) Changes in myocardial oxygenation and perfusion under pharmacological stress with dipyridamole: assessment using T*2 and T1 measurements. Magn Reson Med 41: 686–695.
16. Wacker CM, Hartlep AW, Pfleger S, Schad LR, Ertl G, et al. (2003) Susceptibility-sensitive magnetic resonance imaging detects human myocardium supplied by a stenotic coronary artery without a contrast agent. J Am Coll Cardiol 41: 834–840.
17. Vohringer M, Flewitt JA, Green JD, Dharmakumar R, Wang J Jr., et al. (2010) Oxygenation-sensitive CMR for assessing vasodilator-induced changes of myocardial oxygenation. J Cardiovasc Magn Reson 12: 20.
18. Li D, Dhawale P, Rubin PJ, Haacke EM, Gropler RJ (1996) Myocardial signal response to dipyridamole and dobutamine: demonstration of the BOLD effect using a double-echo gradient-echo sequence. Magn Reson Med 36: 16–20.
19. Egred M, Waiter GD, Al-Mohammad A, Semple SI, Redpath TW, et al. (2006) Blood oxygen level dependent (BOLD) MRI: A novel technique for the detection of myocardial ischemia. Eur J Intern Med 17: 551–555.
20. Wacker CM, Bock M, Hartlep AW, Bauer WR, van Kaick G, et al. (1999) BOLD-MRI in ten patients with coronary artery disease: evidence for imaging of capillary recruitment in myocardium supplied by the stenotic artery. MAGMA 8: 48–54.
21. Utz W, Jordan J, Niendorf T, Stoffels M, Luft FC, et al. (2005) Blood oxygen level-dependent MRI of tissue oxygenation: relation to endothelium-dependent and endothelium-independent blood flow changes. Arterioscler Thromb Vasc Biol 25: 1408–1413.
22. Tanner MA, He T, Westwood MA, Firmin DN, Pennell DJ (2006) Multi-center validation of the transferability of the magnetic resonance T2* technique for the quantification of tissue iron. Haematologica 91: 1388–1391.
23. Pepe A, Positano V, Santarelli MF, Sorrentino F, Cracolici E, et al. (2006) Multislice multiecho T2* cardiovascular magnetic resonance for detection of the heterogeneous distribution of myocardial iron overload. J Magn Reson Imaging 23: 662–668.
24. Modell B, Khan M, Darlison M, Westwood MA, Ingram D, et al. (2008) Improved survival of thalassaemia major in the UK and relation to T2* cardiovascular magnetic resonance. J Cardiovasc Magn Reson 10: 42.
25. Ramazzotti A, Pepe A, Positano V, Scattini B, Santarelli MF, et al. (2008) Standardized T2* map of a normal human heart to correct T2* segmental artefacts; myocardial iron overload and fibrosis in thalassemia intermedia versus thalassemia major patients and electrocardiogram changes in thalassemia major patients. Hemoglobin 32: 97–107.
26. Mavrogeni S, Pepe A, Lombardi M (2011) Evaluation of myocardial iron overload using cardiovascular magnetic resonance imaging. Hellenic J Cardiol 52: 385–390.
27. Pennell DJ, Porter JB, Cappellini MD, Chan LL, El-Beshlawy A, et al. (2011) Continued improvement in myocardial T2* over two years of deferasirox therapy in beta-thalassemia major patients with cardiac iron overload. Haematologica 96: 48–54.
28. Carpenter JP, He T, Kirk P, Roughton M, Anderson LJ, et al. (2011) On T2* magnetic resonance and cardiac iron. Circulation 123: 1519–1528.
29. Modell B, Khan M, Darlison M, Westwood MA, Ingram D, et al. (2008) Improved survival of thalassaemia major in the UK and relation to T2* cardiovascular magnetic resonance. J Cardiovasc Magn Reson 10: 42.

30. Kirk P, He T, Anderson LJ, Roughton M, Tanner MA, et al. (2010) International reproducibility of single breathhold T2* MR for cardiac and liver iron assessment among five thalassemia centers. J Magn Reson Imaging 32: 315–319.

31. Meloni A, Positano V, Keilberg P, De Marchi D, Pepe P, et al. (2012) Feasibility, reproducibility, and reliability for the T*(2) iron evaluation at 3 T in comparison with 1.5 T. Magn Reson Med 68: 543–551.

32. Restaino G, Meloni A, Positano V, Missere M, Rossi G, et al. (2011) Regional and global pancreatic T*2 MRI for iron overload assessment in a large cohort of healthy subjects: normal values and correlation with age and gender. Magn Reson Med 65: 764–769.

33. Turner R, Jezzard P, Wen H, Kwong KK, Le Bihan D, et al. (1993) Functional mapping of the human visual cortex at 4 and 1.5 tesla using deoxygenation contrast EPI. Magn Reson Med 29: 277–279.

34. van der Zwaag W, Francis S, Head K, Peters A, Gowland P, et al. (2009) fMRI at 1.5, 3 and 7 T: characterising BOLD signal changes. Neuroimage 47: 1425–1434.

35. Donahue MJ, Hoogduin H, van Zijl PC, Jezzard P, Luijten PR, et al. (2011) Blood oxygenation level-dependent (BOLD) total and extravascular signal changes and DeltaR2* in human visual cortex at 1.5, 3.0 and 7.0 T. NMR Biomed 24: 25–34.

36. Thalhammer C, Renz W, Winter L, Hezel F, Rieger J, et al. (2012) Two-Dimensional sixteen channel transmit/receive coil array for cardiac MRI at 7.0 T: Design, evaluation, and application. J Magn Reson Imaging 36: 847–857.

37. Winter L, Hezel F, Renz W, Grassl A, Hezel F, et al. (2012) Comparison of three multichannel transmit/receive radiofrequency coil configurations for anatomic and functional cardiac MRI at 7.0T: implications for clinical imaging. Eur Radiol 22: 2211–2220.

38. Frauenrath T, Hezel F, Heinrichs U, Kozerke S, Utting JF, et al. (2009) Feasibility of cardiac gating free of interference with electro-magnetic fields at 1.5 Tesla, 3.0 Tesla and 7.0 Tesla using an MR-stethoscope. Investigative Radiology 44: 539–547.

39. Frauenrath T, Hezel F, Renz W, d'Orth Tde G, Dieringer M, et al. (2010) Acoustic cardiac triggering: a practical solution for synchronization and gating of cardiovascular magnetic resonance at 7 Tesla. J Cardiovasc Magn Reson 12: 67.

40. Reeder SB, Faranesh AZ, Boxermann JL, McVeigh ER (1998) In vivo measurement of T$_2$* and field inhomogeneity maps in the human heart at 1.5 T. Magn Reson Med 39: 988–998.

41. Christ A, Kainz W, Hahn EG, Honegger K, Zefferer M, et al. (2010) The Virtual Family—development of surface-based anatomical models of two adults and two children for dosimetric simulations. Physics in medicine and biology 55: N23.

42. Griswold MA, Jakob PM, Heidemann RM, Nittka M, Jellus V, et al. (2002) Generalized autocalibrating partially parallel acquisitions (GRAPPA). Magn Reson Med 47: 1202–1210.

43. Shah S, Kellman P, Greiser A, Weale P, Zuehlsdorff S, et al. (2009) Rapid Fieldmap Estimation for Cardiac Shimming. Proc Intl Soc Mag Reson Med 17: 566.

44. Schär M, Kozerke S, Boesiger P (2004) Navigator gating and volume tracking for double-triggered cardiac proton spectroscopy at 3 Tesla. Magn Reson Med 51: 1091–1095.

45. Cerqueira M, Weissman N, Dilsizian V, Jacobs A, Kaul S, et al. (2002) Standardized myocardial segmentation and nomenclature for tomographic imaging of the heart: a statement for healthcare professionals from the Cardiac Imaging Committee of the Council on Clinical Cardiology of the American Heart Association. Circulation 105: 539–542.

46. (2010) International Electrical Commission: Particular requirements for the basic safety and essential performance of magnetic resonance equipment for medical diagnosis. IEC-60601-2-33 Medical electrical equipment Part 2–33.

47. Smith GC, Carpenter JP, He T, Alam MH, Firmin DN, et al. (2011) Value of black blood T2* cardiovascular magnetic resonance. J Cardiovasc Magn Reson 13: 21.

48. Schar M, Kozerke S, Fischer SE, Boesiger P (2004) Cardiac SSFP imaging at 3 Tesla. Magn Reson Med 51: 799–806.

49. Schar M, Vonken EJ, Stuber M (2010) Simultaneous B(0)- and B(1)+-map acquisition for fast localized shim, frequency, and RF power determination in the heart at 3 T. Magn Reson Med 63: 419–426.

50. Pan JW, Lo KM, Hetherington HP (2012) Role of very high order and degree B(0) shimming for spectroscopic imaging of the human brain at 7 tesla. Magn Reson Med 68: 1007–1017.

51. Hetherington HP, Avdievich NI, Kuznetsov AM, Pan JW (2010) RF shimming for spectroscopic localization in the human brain at 7 T. Magn Reson Med 63: 9–19.

52. Ziener CH, Kampf T, Melkus G, Jakob PM, Schlemmer HP, et al. (2012) Signal evolution in the local magnetic field of a capillary – analogy to the damped driven harmonic oscillator. Magn Reson Imaging 30: 540–553.

53. Reichenbach JR, Haacke EM (2001) High-resolution BOLD venographic imaging: a window into brain function. NMR Biomed 14: 453–467.

54. Reese TG, Weisskoff RM, Smith RN, Rosen BR, Dinsmore RE, et al. (1995) Imaging myocardial fiber architecture in vivo with magnetic resonance. Magn Reson Med 34: 786–791.

55. Wu MT, Tseng WY, Su MY, Liu CP, Chiou KR, et al. (2006) Diffusion tensor magnetic resonance imaging mapping the fiber architecture remodeling in human myocardium after infarction: correlation with viability and wall motion. Circulation 114: 1036–1045.

56. O'Regan D, Callaghan M, Fitzpatrick J, Naoumova R, Hajnal J, et al. (2008) Cardiac T2* and lipid measurement at 3.0 T-initial experience. Eur Radiol 18: 800–805.

57. Meloni A, Luciani A, Positano V, De Marchi D, Valeri G, et al. (2011) Single region of interest versus multislice T2* MRI approach for the quantification of hepatic iron overload. J Magn Reson Imaging 33: 348–355.

58. He T, Gatehouse PD, Kirk P, Tanner MA, Smith GC, et al. (2007) Black-blood T2* technique for myocardial iron measurement in thalassemia. J Magn Reson Imaging 25: 1205–1209.

59. Tsaftaris SA, Rundell V, Zhou X, Liu Y, Tang R, et al. Detecting Myocardial Ischemia at Rest with Cardiac Phase-Resolved BOLD MRI: Early Findings. Proc Intl Soc Mag Reson Med; 2011; Montreal, Quebec, Canada. #217.

60. Dharmakumar R, Arumana JM, Tang R, Harris K, Zhang Z, et al. (2008) Assessment of regional myocardial oxygenation changes in the presence of coronary artery stenosis with balanced SSFP imaging at 3.0 T: theory and experimental evaluation in canines. J Magn Reson Imaging 27: 1037–1045.